Research Article Vol. 10, No. 1 / January 2023 / Optica 1

Ultrafast quantum dynamics driven by the strong space-charge field of a relativistic electron beam

D. Cesar,[1,*] A. Acharya,[1] J. P. Cryan,[1,2] A. Kartsev,[1,3,4] M. F. Kling,[1,2,5] A. M. Lindenberg,[1,2,6,7] C. D. Pemmaraju,[7,8] A. D. Poletayev,[1,6,7,9] V. S. Yakovlev,[10,11] and A. Marinelli[1]

[1]SLAC National Accelerator Laboratory, Menlo Park, California 94025, USA
[2]Stanford PULSE Institute, SLAC National Accelerator Laboratory, Menlo Park, California 94025, USA
[3]Bauman Moscow State Technical University, Moscow, 105005, Russia
[4]Computing Center of the Far Eastern Branch of the Russian Academy of Sciences, 680000 Khabarovsk, Russia
[5]Department of Applied Physics, Stanford University, Stanford, California 94305, USA
[6]Department of Materials Science and Engineering, Stanford University, Stanford, California 94305, USA
[7]Stanford Institute for Materials and Energy Sciences, SLAC National Accelerator Laboratory, Menlo Park, California 94025, USA
[8]Theory Institute for Materials and Energy Spectroscopies, SLAC National Accelerator Laboratory 94025, Menlo Park, California 94025, USA
[9]Current Address: Department of Materials, University of Oxford, Oxford OX13RQ, UK
[10]Max Planck Institute of Quantum Optics, 85748 Garching, Germany
[11]Department of Physics, Ludwig-Maximilians-Universität Munich, 85748 Garching, Germany
*Corresponding author: dcesar@slac.stanford.edu

Received 26 July 2022; revised 10 October 2022; accepted 12 October 2022; published 21 December 2022

In this paper, we illustrate how the Coulomb field of a highly relativistic electron beam can be shaped into a broadband pulse suitable for driving ultrafast and strong-field physics. In contrast to a solid-state laser, the Coulomb field creates a pulse that can be intrinsically synchronized with an x-ray free electron laser (XFEL), can have a cutoff frequency broadly tunable from THz to extreme ultraviolet (EUV), and that acts on target systems as a "half-cycle" impulse. Explicit examples are presented to emphasize how the unique features of this excitation can be a tool for novel science at XFEL facilities such as the Linac Coherent Light Source (LCLS).

https://doi.org/10.1364/OPTICA.471773

1. INTRODUCTION

Over the last decade, x-ray free electron lasers (XFELs) have been a transformative tool for the physical sciences by delivering intense bursts of x rays that can probe electronic structures with site specificity and ultrafast temporal resolution [1]. The high intensity of the XFEL allows the pump–probe framework to be applied to traditional x-ray imaging and spectroscopy, where the pump is most often either a secondary x-ray pulse [2–4] or a solid-state laser that has been synchronized to the x-ray probe [5–7]. More recently, novel electron-beam shaping techniques have extended XFEL temporal resolution to the attosecond regime and made it possible to chart coherent charge dynamics in molecular systems [8,9].

In this paper, we propose to extend the reach of ultrafast science at XFELs by directly pumping quantum systems with the same relativistic electron beam used to generate x rays [Fig. 1(a)]. The beam interacts with valence electrons primarily through the optical cross section (rather than the comparatively small collisional cross section [44]), such that we can think of its Coulomb field as a strong, "half-cycle," radially polarized laser. Pioneering experiments at the Sub-Picosecond Pulse Source (SPPS) [45] and FACET [46] facilities demonstrate that this beam field can be used to drive magnetic switching [47,48] and ultrafast changes in conductivity [49].

More generally, the field of the beam is an ultra-broadband impulse that drives processes ranging from "DC"-like Stark shifts up to ultraviolet (UV) ionization of valence electrons. The resulting dynamics are a complex superposition of excited states most similar to those created by single-cycle THz sources [Fig. 1(b)]; however, we identify four main distinctions: first, the pulse length can be much shorter than that of conventional lasers; indeed, by using techniques developed to produce attosecond x rays [50,51], we can create half-cycle fields with intensity profiles as short as 250 as, corresponding to a 12 eV bandwidth. Second, the field is truly a "unipolar" impulse, such that the direct momentum transfer $A = -\int E\mathrm{d}t$ is nonzero. Third, we can create strong fields up to tens of V/Å by focusing the electron beam to sub-wavelength spot sizes. And, last, the field is intrinsically synchronized to the x-ray pulses generated by the bunch.

The importance of the last point should not be underestimated: state-of-the-art timing jitter between an optical laser and an XFEL pulse is between 20 and 100 fs [52], such that time-stamping techniques must be used to re-sort data on a shot-by-shot basis [53]—a feat that will become increasingly difficult as the next generation

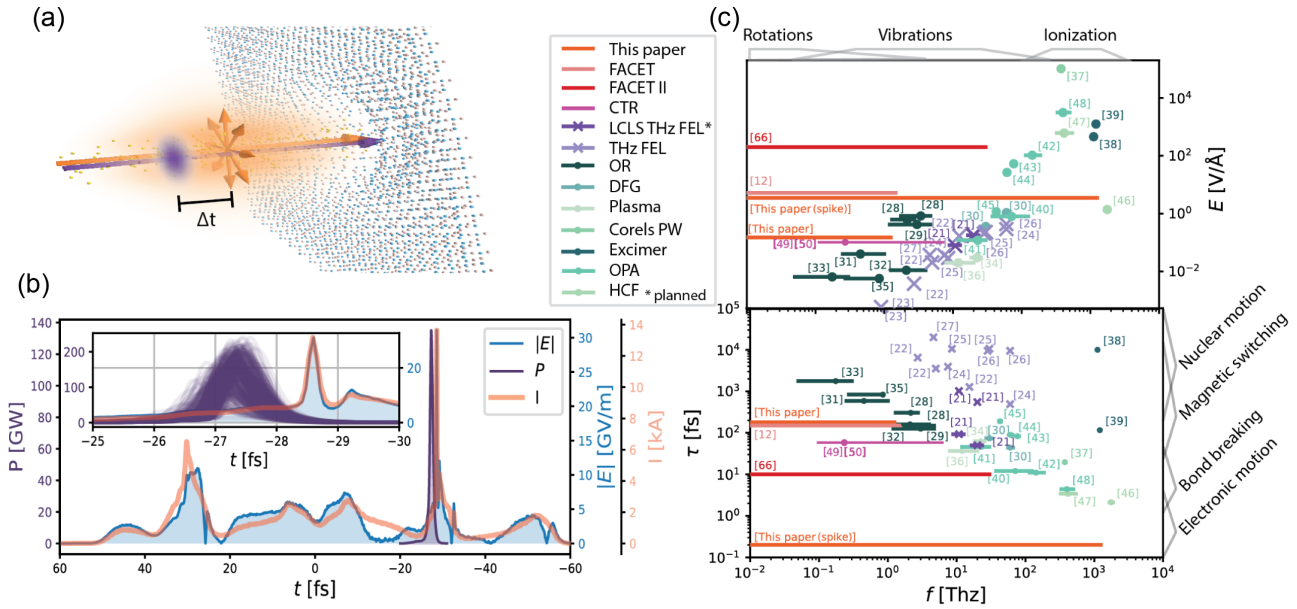

Fig. 1. Parameter space for Coulomb driven quantum dynamics. (a) Graphic of a space-charge pump, x-ray probe experiment. (b) Space-charge field (blue), electron beam current (red), and power of sample XFEL pulses (shown here after at a particular pump–probe delay) (purple) from start-to-end simulations of the LCLS-II CuS beamline. (c) Parameter space plots comparing conventional FEL [10–16] and laser sources to beam driven fields (including CTR, coherent transition radiation [38,39]). OR, optical rectification; DFG, difference frequency generation; PW, petawatt; OPA, optical parametric amplification; HCF, hollow core fiber [17–37]. The references follow those of topical reviews [40–42]. Notice that the conventional sources appear to lie along lines (in the log–log plot) because increasing frequency implies a smaller diffraction-limited spot size [43]. The space-charge fields violate this trend because an electron beam can be focused to sub-wavelength spot sizes (here, we chose 20 μm rms as a compromise between pumped volume and field strength). The resulting beam driven fields have a wider bandwidth (FWHM in intensity), shorter duration (FWHM in intensity), and larger field strength (peak) than their conventional counterparts.

of high rate superconducting FELs come online. Intrinsic synchronization bypasses this issue and directly enables attosecond pump–probe experiments.

In this paper, we discuss how to generate, characterize, and ultimately use ultrafast space-charge and x-ray pulses for photon–electron pump–probe experiments (PEPPEx). Our discussion is grounded by start-to-end simulations at the Linac Coherent Light Source (LCLS)-II CuS beamline [54], although the same concepts are adaptable to other FEL beamlines. We show how the electron beam's phase space can be manipulated with a laser heater to produce two spikes suitable for a pump–probe experiment. We calculate the x-ray and space-charge fields from this beam, and we show how photo-electron streaking can be used to reconstruct those same fields. Then we discuss the interaction of the space-charge field with three distinct quantum systems.

2. PULSE SYNTHESIS

To prepare an ultrafast pump–probe experiment, we first shape the electron beam to have two short current spikes: the latter ("tail") spike is used to generate x rays, while the former ("head") spike is used for its Coulomb field. A small magnetic chicane can then be used to delay the electron beam relative to the x rays and precisely set the overlap between the Coulomb field and the x-ray pulse. To optimize this arrangement, it is necessary to control the chirp of the two current spikes separately, since the Coulomb spike should be fully compressed, while the lasing spike should be strongly chirped (the addition of an x-ray delay line would create additional flexibility, but we do not use one here).

One method to create such a bunch is based on laser heater shaping, as described in detail in [55]. In short, the process plays out as illustrated in Fig. 2, which is based on start-to-end simulations of the LCLS-II CuS beamline [54] (using IMPACT-T for the injector and Elegant for the transport from the injector to the undulators [56–58]). First, a stack of Gaussian laser heater pulses creates a time-dependent slice-energy spread. Then, after the first bunch compressor, the energy spread is converted into current modulations that seed the microbunching instability and are amplified during transport. Next, anomalous dispersion in the magnetic dogleg compresses the space-charge induced chirp into two large current spikes. The energy spread is enhanced by the impedance of a large K wiggler, as in [10], before final compression of the head spike in the delay chicane. The final chicane compresses only the tail of the microbunch, where the nonlinear space-charge impedance has the correct sign for compression. The compression ratio of the two spikes can be controlled separately by changing the delay between successive heater pulses (relative to both each other and the beam center) to optimize the microbunching gain for each spike separately.

This procedure leaves us with a strongly chirped tail spike that we use to generate the x-ray probe by matching the undulator taper to the beam chirp [8,50]. Genesis [59] simulations based on the LCLS-II soft x-ray line [54] show that, with a matched taper, the tail spike can produce 450 eV soft x rays with an average power over 120 GW, compared to <10 GW from the head spike. The inset in Fig. 1(b) shows many individual simulations of the tail spike, each with a unique random seed leading to unique FEL dynamics. Most often the individual pulses have a 0.6 fs full-width-at-half-maximum (FWHM) pulse length, but varying amounts of

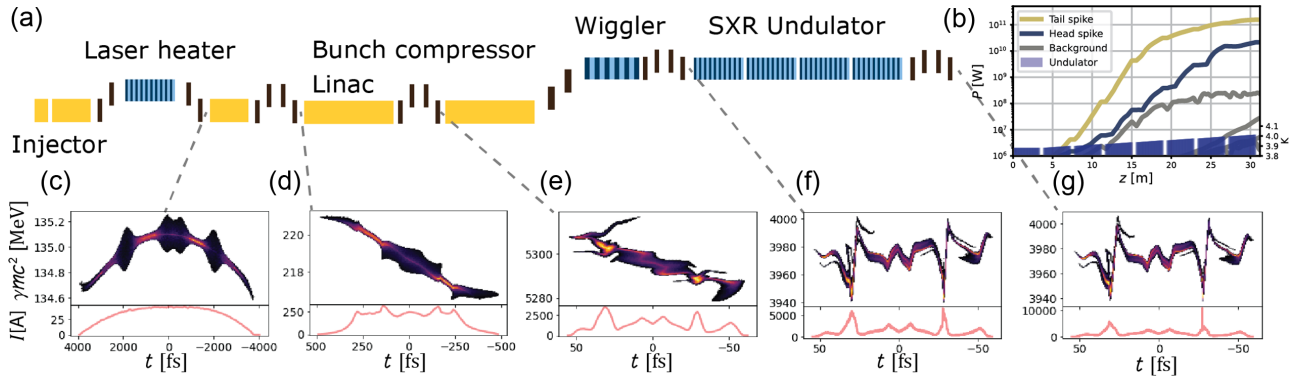

Fig. 2. (a) Graphic of the LCLS-II CuS beamline. (c)–(g) Snapshots of the electron beam longitudinal phase space. A coherent energy modulation is applied by a stack of 0.7 ps long laser heater pulses. This modulation evolves into two large spikes separated by approximately 50 fs. The undulator (450 eV) is chirp-taper matched to the tail (left) spike so that the (ensemble averaged) peak power (b) from the tail grows fastest and dominates the total x-ray radiation.

post-saturation slippage broaden the ensemble-averaged intensity to 0.8 fs FWHM. This 0.2 fs difference is expected to be the dominant component of the pump–probe jitter between the x rays and the electron beam.

After lasing, a 40 fs chicane delay overlaps the x-ray pulse with the current spike at the head of the bunch, as shown in Fig. 1(b). At the same time, this chicane fully compresses the head spike into a 13.5 kA peak with a FWHM width of only 250 as and an energy spread of 25 MeV. A long pedestal accompanies both sides of the current spike. Small changes in dispersion from the chicane can be used to control the pump–probe delay within an effective Rayleigh length coorsponding to ≈ 35 fs of pump–probe delay (outside of which the current spike begins to de-compress). Note also that the head spike loses a small, but variable, amount of energy while lasing, and this leads to negligible jitter (compared to rf induced jitter) in the compressed spike width—the current profile in Fig. 1(b) shows a typical case.

The electrons in our beam collectively form a strong electromagnetic impulse that closely approximates a half-cycle laser pulse. For a transversely Gaussian charge density, we can estimate the electric field as

$$\rho_\perp = \frac{I(t)}{2\pi\sigma_r^2} e^{-\frac{1}{2}\left(\frac{r}{\sigma_r}\right)^2},$$

$$\boldsymbol{E}(\boldsymbol{r}, t) = \hat{r}\frac{Z_0 I(t)}{2\pi r}\left(1 - e^{-\frac{1}{2}\left(\frac{r}{\sigma_r}\right)^2}\right), \quad (1)$$

with an associated azimuthal magnetic field given by $\boldsymbol{B} = (\boldsymbol{\beta} c \times \boldsymbol{E})$. This model for the field produced by the beam is valid provided that: (a) we consider only frequencies commensurate with the bunch length $f \lesssim 1/\sigma_t$, such that the field of the individual electrons add coherently, and we can neglect stochastic effects [44,60]; (b) we consider only cases in which the beam can be approximated by a long cylinder in its rest frame: $\sigma_r < \gamma c \sigma_t$; and finally (c), that the beam density is a 1D Gaussian cylinder. Of these conditions, only (c) is regularly violated in practice. In particular, while an individual slice of the electron beam may resemble a Gaussian cross section, the centroid is often a strong function of t due to coherent synchrontron radiation (CSR) induced energy loss in the bunch compressor. Thus, to get an accurate space-charge field, we use the numerical Poisson solver from the tracking code GPT [61]. It is this field, evaluated at a single point in space, that is plotted as the blue curve in Fig. 1(b).

One implication of Eq. (1) is that the space-charge field can be very large when the electron beam is tightly focused. For this paper, we choose a 20 μm (rms) beam size: 20 μm is much smaller than a free space THz laser could be focused, but it is still large enough to be easily resolved by a soft x-ray probe. It is precisely this fact that allows us to access the strong-field THz part of the parameter space in Fig. 1. At the same time, the strongest fields are achieved when the sample overlaps with the electron beam. Consequently, there will be "close" binary encounters not described by Eq. (1) {Eq. (1) is the coherent sum of the "far" collisions that can be described by the Weizsacker–Williams method [44]} that lead to impact ionization with a cross section (in the relativistic limit) of $\sigma_{\mathrm{MRBEB}} \approx 2\pi r_e^2 n (m_e c^2/E_i) \ln\gamma$ [62], where r_e is the classical electron radius, E_i is the bound state ionization energy, n is the bound state occupation number, and $m_e c^2$ is the electron rest mass. The chance of a single molecule in the sample undergoing a close collision with the beam is then roughly $\sigma_{\mathrm{MRBEB}} N_e/(\pi\sigma_r^2) \lessapprox 10^{-6}$ (where N_e is the number of electrons in the beam). Thus, while close collisions will make some high energy radiation shower (which FEL facilities are designed to shield from the x-ray detectors), they will not cause a significant fraction of the sample to be excited.

3. PULSE CHARACTERIZATION

The "gold standard" for the metrology of sub-femtosecond EUV and x-ray pulses is photoemission streaking with long wavelength fields. In this technique, an ultrashort laser pulse is overlapped with a longer wavelength dressing laser field. The combined field is incident on a gas sample, and the momentum distribution of electrons ionized by the ultrashort field is displaced ("streaked") by the long-wavelength dressing field [63–65]. This two-color ionization process encodes the information of the short-wavelength pulse into the measured photo-electron momentum distribution. The pulse profiles can be retrieved from the resultant spectrogram (recorded by scanning the relative delay between the x-ray pulse and IR field) via a number of proposed algorithms [66–69]. To date, streaking at XFEL facilities relies on an external laser pulse that must be overlapped with the XFEL pulse inside a gas phase sample. The shot-to-shot jitter of the relative laser/x-ray arrival

time precludes measurements that are not single shot, and thus the dressing field has always been either long wavelength [70] or circularly polarized [8,71,72]. But by using a naturally synchronized, unipolar streaking field, we have the possibility to average together many independent shots and thus greatly increase measurement sensitivity.

Streaked photo-electron spectra are conventionally calculated within the strong field approximation to the Schrödinger equation for a single active electron, which ignores the effect of the Coulomb potential on the emitted electron. In this approximation, the probability for observing an electron with momentum $\boldsymbol{k}$ is given by

$$W(\boldsymbol{k},\tau)=\left|\int_{-\infty}^{\infty}\mathrm{d}t e^{i(Q(t))}D(\boldsymbol{k}+\boldsymbol{A}(\boldsymbol{t}))\boldsymbol{E}_x(t-\tau)\right|^2, \quad (2)$$

$$Q(t)=\int_{-\infty}^{t}\mathrm{d}t'\left(\mathrm{IP}+\frac{1}{2}(\boldsymbol{k}+\boldsymbol{A}(t'))^2\right), \quad (3)$$

where $D(\boldsymbol{k})$ is the photoionization dipole moment (here, approximated with the value for hydrogen atoms $D(\boldsymbol{k})=\frac{\boldsymbol{k}}{(k^2+2\mathrm{IP})^3}$), IP is the ionization potential, $\boldsymbol{E}_x(t')$ is the electric field of the ionizing x-ray pulse, and $A(t)=-\int \mathrm{d}t E(t)$ is the vector potential of the streaking (space-charge) field with $A(\infty)=0$. $Q(t)$ is the so-called Volkov phase. In anticipation of averaging over many shots, we will re-write this in terms of the first-order correlation function $\boldsymbol{\Gamma}(t_1,t_2)=\langle E(t_1)E^*(t_2)\rangle$, which allows us to account for the self amplified spontaneous emission (SASE) jitter:

$$W(\boldsymbol{k},\tau)=\int_{-\infty}^{\infty}\int_{-\infty}^{\infty}\mathrm{d}t_1\mathrm{d}t_2 e^{i(Q(t_1)-Q(t_2))}D(\boldsymbol{k}+\boldsymbol{A}(\boldsymbol{t_1}))\times D^*(\boldsymbol{k}+\boldsymbol{A}(\boldsymbol{t_2}))\boldsymbol{\Gamma}(t_1-\tau,t_2-\tau). \quad (4)$$

Within the quasi-classical model, we imagine that an ionizing x-ray pulse creates photo-electrons at time t_i with probability $I(t)$ (intensity of the incident x-ray pulse) and energy $\frac{k^2}{2}$ with probability $I(w)$ (possibly with some $t-\omega$ correlation due to chirp). If the streaking field is strong, then the Coulomb potential can be neglected, and the now-free electrons are accelerated to a final momentum of $\boldsymbol{k}_f=\boldsymbol{k}_i-\boldsymbol{A}$.

In Fig. 3, we simulate a spectrogram $W(k,\tau)$ based on the fields from the previous section (for photo-electrons emitted from a single point in space and collected parallel to the x-ray polarization). For each time delay, we average the spectrum from Eq. (2) calculated using many independent random seeds for the SASE radiation (but neglecting any changes in A due to machine jitter). The quasi-classical model allows a straightforward interpretation: we see two distinct populations separated by $2k_i=2\sqrt{2(\hbar\omega-\mathrm{IP})}$ for an ionization potential IP, corresponding to electrons emitted in directions parallel and anti-parallel to the streaking field. Each group of electrons then follows the vector $A(t)$ as the pump–probe delay is changed. Where the streaking field is large, the spectral width of the photo-electron peak is proportional to its pulse duration, and where the streaking field is weak, it is proportional to the x-ray spectrum. In between, as we can see in the inset in Fig. 3, the widths of the parallel and anti-parallel populations are different, due the average chirp of the x-ray beam (originating from the chirp-taper FEL configuration [8]).

After averaging over many shots to produce a spectrogram, we are no longer sensitive to the pulse length of individual shots. Instead, we measure the first order correlation function $\Gamma(t_1,t_2)$, as indicated by Eq. (4). An example $\Gamma(t_1,t_2)$ calculated directly from the FEL simulations is shown in Fig. 3(b): the main diagonal ($t_1=t_2$) yields the average FEL power, while the off-diagonals ($t_1\propto -t_2$) are related to the coherence length. Because the FEL is not a stationary process, the coherence length is not constant, but in fact increases towards the head (upper right) of the pulse, where the slippage has built up coherent power.

To fully reconstruct $\Gamma(t_1,t_2)$ and the streaking field $A(t)$, we adopt a procedure similar to [69,73], in which we first estimate the streaking field based on the average spectrum $A(t)\approx\langle W(\tau)\rangle|_k$ and then iteratively solve the least squares problem for $\Gamma(t_1,t_2)$ [i.e., Eq. (4)]. This avoids the approximations used in common frequency-resolved optical gating for complete reconstruction of attosecond bursts (FROG-CRAB) algorithms, which are not applicable to our case. To speed up convergence, we represent the underlying Γ in a compact basis, an extension of the von Neumann basis used in [73]. We can then refine our guess for $A(t)$ because we know that, within the quasi-classical approximation, the average spectrum is the convolution of the streaking field and the average x-ray power: $\langle W(\tau)\rangle|_k=A(\tau)\circledast\Gamma(\tau,\tau)$. We demonstrate this technique in Figs. 3(b)–3(d), where we have calculated Γ once, using only the portion of the spectrum between 25 and 15 fs, where

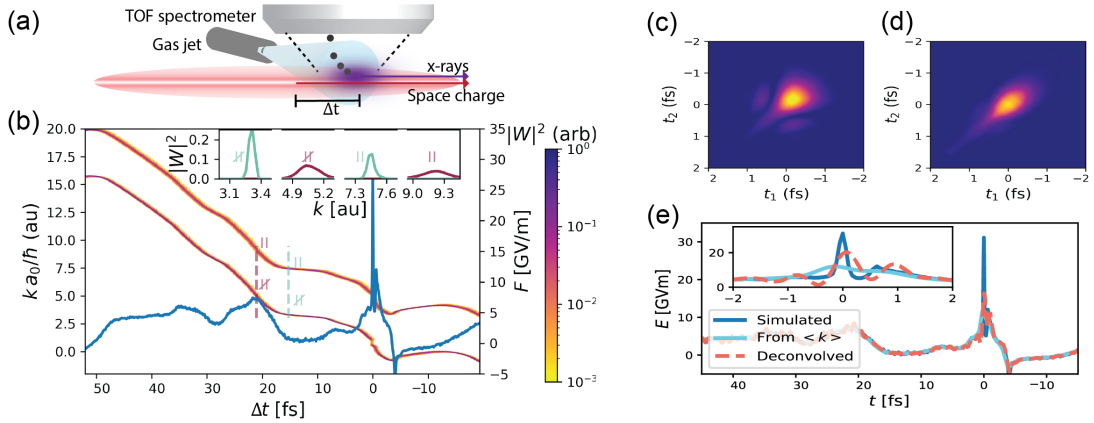

Fig. 3. Ultrafast pulse metrology by photo-electron streaking. (a) Graphic of the streaking measurement. (b) Spectrogram showing the photo-electron spectrum as a function of pump–probe delay. Also shown is the streaking field (blue). The inset shows the spectrum measured at two time delays as indicated by the dashed lines. (c) Simulated correlation function $\Gamma(t_1,t_2)$. (d) Reconstructed correlation function. (e) Simulated and reconstructed Coulomb fields.

our assumption of slowly changing A is well justified. Finally, we improve our guess of A by de-convolution with $\Gamma(\tau, \tau)$.

The reconstruction of $\Gamma(\tau, \tau)$ quickly converges to the correct average power. It also captures the increasing coherence length towards the head of the pulse. However, the simulated $\Gamma(\tau, \tau)$ shows small coherent satellites near the tail (corresponding to pulse splitting), which are not recovered in this reconstruction. To capture these weak features, one could create a spectrogram with higher precision in k and a larger range of streaking fields, but in practice, resolving such weak features will be difficult. Further iteration including non-linear optimization of A (as in [69]) can improve the reconstruction of the sharp current spike near $t = 0$, but at the cost of significant computational resources.

Once the streaking amplitude is well calibrated from an average spectrogram, it is possible to estimate single-shot FEL pulse lengths from streaked spectra. To do so accurately, one should set the pump–probe delay such that the streaking field is large and the x-ray spectrum is negligible. Where this is not possible, one can still make an estimate of single-shot parameters, especially if both the parallel and anti-parallel bunches can be gathered and the x-ray spectrum measured downstream (since a comparison of the two gives direct information about the x-ray chirp).

4. BEAM DRIVEN QUANTUM DYNAMICS

The relativistic electron beam is a uniquely broadband pump pulse that is both faster and stronger than comparable single-cycle pulses (see Fig. 1). It can excite electronic transitions, shift electronic energy levels, and drive large-scale nuclear motion. The pulses are fast enough that they can act impulsively [74], and yet strong enough to manipulate wave packet dynamics.

The wide range of quantum dynamics triggered by the electron beam pump can be tuned by altering the space-charge field's cutoff frequency and field strength. We consider two cases [Fig. 1(b)]: a 250 as 12 kA current spike, and a 250 fs 1 kA flattop electron beam. The current spike contains 4 μJ within its FWHM profile and extends out to 12 eV at 3.5 V/Å, while the flattop beam contains 11 μJ within its FWHM profile and extends out to 1 THz at 0.15 V/Å. Both beams are focused to 20 μm (rms) spot size as a compromise between pumped-volume and field strength. If an ion microscope is used to spatially resolve the pumped volume [75], then the beams could be designed with a tighter focus to further increase the field strength. Indeed, at FACET-II, a tighter focus and stronger compression are expected to push beam driven fields into the regime of relativistic optics and quantum electrodynamics (QED) [76].

The resulting physics can be directly probed by the intrinsically synchronized XFEL pulse. In the attosecond modality discussed in the previous sections, which builds on previous work at LCLS [8,9], we imagine using soft-x ray absorption spectroscopy to make a chemically resolved diagnostic of ultrafast motion. But it is also possible to measure structural changes directly from x-ray diffraction. In either case, the x-ray probe provides mechanistic insight into the ultrafast dynamics that cannot easily be obtained from an optical probe.

Here we discuss three pump–probe scenarios that highlight the flexibility of the electron beam pump source. First, we consider photochemical reactions pumped by the EUV spectral component of an attosecond current spike. Second, we consider electronic transitions in a large bandgap dielectric where an attosecond current spike causes direct ionization to the conduction band and then a long THz-like pedestal accelerates the free carriers. Finally, we discuss using a long flattop electron beam to drive large-amplitude ion motion in the model battery solid electrolyte Na β/β'' alumina. For this case, we estimate how soft-x-ray absorption can be used to track large excursions in the mobile Na ion density and thus create a pathway towards a mechanistic understanding of ionic conductivity and its vibrational origins.

A. Ultrafast Photochemistry

Ultrafast photochemistry provides opportunities for improving our understanding of synthetic chemistry and energy storage by delivering energy directly to a target molecule in an otherwise cold system. The current spike simulated in this paper can drive the electronic excitation significantly faster than conventional UV lasers, which allows us to selectively probe ultrafast reaction pathways. It is difficult, however, to predict the photochemical reactivity based on the reactant structure through structure–reactivity relationships (in all but the simplest cases). Beyond this, non-adiabatic dynamics near conical intersections (CIs) in excited electronic states involve an interplay of electronic and nuclear degrees of freedom, which cannot be described within the Born–Oppenheimer approximation, and are responsible for much of the excited state behavior in photochemistry. By shaping the current profile of our electron beam, we may be able to exert control over the conical interaction and alter the non-adiabatic dynamics [77–80]. The role of a short current spike in driving photochemical reactions can be thought of as arising from the EUV field associated with the electromagnetic field of the beam. We visualize this effect in Fig. 4 for the 250 as spike, shown in Fig. 2 by calculating the time–frequency Wigner–Ville distribution of the electric field. The short spike in the beam leads to a 250 as window with spectral content out to 12 eV. The pedestal accompanying that short spike can cause strong-field ionization if the beam is focused too tightly, but in the perturbative regime, it simply causes a Stark shift of the energy levels. In this case, the ultrafast spike can transition valence electrons into excited states on an impulsive time scale.

When targeting lower energy transitions, it is possible to tune the EUV cutoff by using bunches of different lengths. For example, if the current spike is removed entirely, then the cutoff frequency will move to the Thz regime (shown by the orange curve in Fig. 2). Alternatively, it is possible to reduce the zero-frequency component by tilting the beam [81] so that the head passes to one side of the probe region and the tail to the other side, forming a single-cycle rather than half-cycle pulse.

B. Electronic Dynamics in a Model Dielectric

Studies of light–matter interaction at the ultrafast time scale can give unique insight into the optoelectronic properties and device physics of emerging materials. Specifically, the charge-carrier dynamics following light excitation have direct implications for optoelectronic device performance in terms of charge-carrier generations, recombination, and charge-transfer processes. High intensity fields can be used to drive electrons far from their equilibrium, leading to Bloch oscillations within each sub-band of a solid and processes such as high harmonic generation [82]. The space-charge field opens a new regime for controlling electron dynamics in solids by providing a strong field that can rapidly

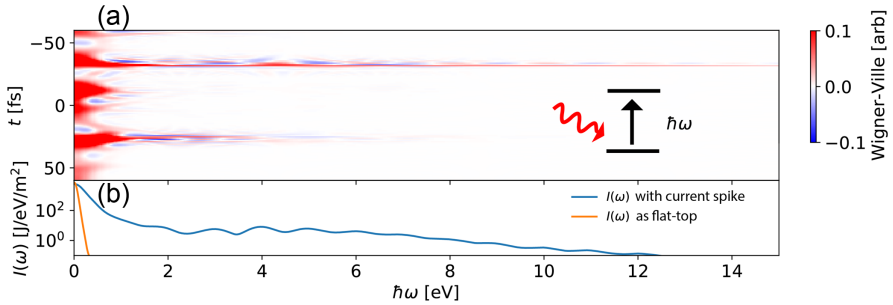

Fig. 4. (a) Wigner–Ville distribution of the Coulomb field. (b) Spectrum of the Coulomb field with and without the current spike. With the current spike, the spectrum extends out well into the EUV where it can directly excite many valence transitions. Without the current spike, the spectrum does not extend beyond the THz frequencies. The compression of the beam can be tuned to control the cutoff frequency.

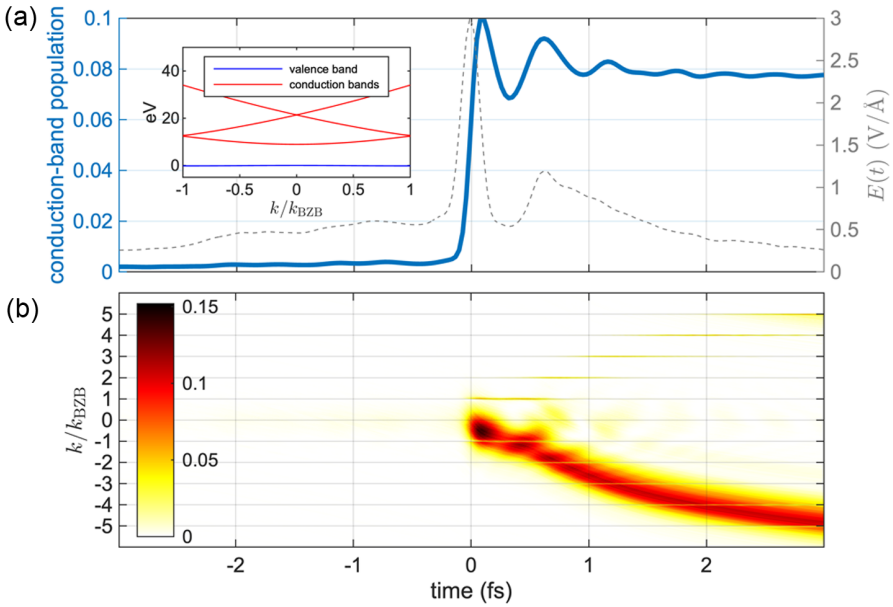

Fig. 5. Interaction of the space-charge field (gray dashed curve) with a one-dimensional periodic lattice potential that has a bandgap of 9 eV (equivalent to the bandgap of crystalline quartz). (a) From the time evolution of the conduction-band population (blue curve), we see that transitions from valence to conduction bands mainly happen during the main spike of the electric field. The inset shows the band structure within the first Brillouin zone ($k_{\mathrm{BZB}} = 0.628\ ^{-1}$). (b) Photo-injected electrons are rapidly accelerated by the space-charge field, crossing multiple Brillouin-zone boundaries (BZB), which promotes them to high conduction bands. While (a) shows the occupation averaged over crystal momenta, this pseudocolor diagram represents the motion of the electron wave packet in reciprocal space, where the bands are unfolded into the extended-zone scheme, and the colors in this diagram represent the occupations of Bloch states in the first five conduction bands.

excite free carriers and drive them to high energies before scattering. Here, as a proof of concept, we have performed simulations on the space-charge field interaction within a dielectric. The dielectric is simplified in our simulations with a one-dimensional periodic lattice potential that has a bandgap of 9 eV, close to the bandgap of crystalline quartz [see Fig. 5(a)]. We solved the time-dependent Schrödinger equation in the basis of accelerated Bloch states, as described in [83]. In this model, all electrons initially occupy valence states in a periodic potential, the parameters of which were identical to those in [84]. The broad spectrum of the space-charge field allows for single-photon transitions across the 9 eV band gap, which are largely confined to the central spike. The spike itself is too short to significantly accelerate the charge carriers that it creates, but the electric field that follows the spike makes electrons acquire kinetic energies of the order of tens of electronvolts. Electrons gain energy by making transitions to higher conduction bands as they cross the Brillouin-zone borders. While Fig. 5(a) shows the occupation averaged over crystal momenta, Fig. 5(b) represents the motion of the electron wave packet in reciprocal space. The simulations show that probing the unfolding changes in charge motion upon excitation by the space-charge field with attosecond time resolution and atomic specificity would open up exciting perspectives in attosecond material science, including the development of petahertz optoelectronic switches.

C. Nuclear Motion in Ionic Conductors

For frequencies up to several THz, the spectral intensities and peak fields of the space-charge field can be more than 10× those of single-cycle tabletop sources [85]. This makes it an attractive strong-field source for triggering lattice dynamics that couple to exotic non-equilibrium phases [86,87] or large-amplitude ionic motions that couple to ionic conduction [88,89]. Soft x-ray radiation from the same electron beam can then provide a chemical resolution to selectively target shifts in the active ions and to probe the time-resolved ion trajectory and associated intermediate states.

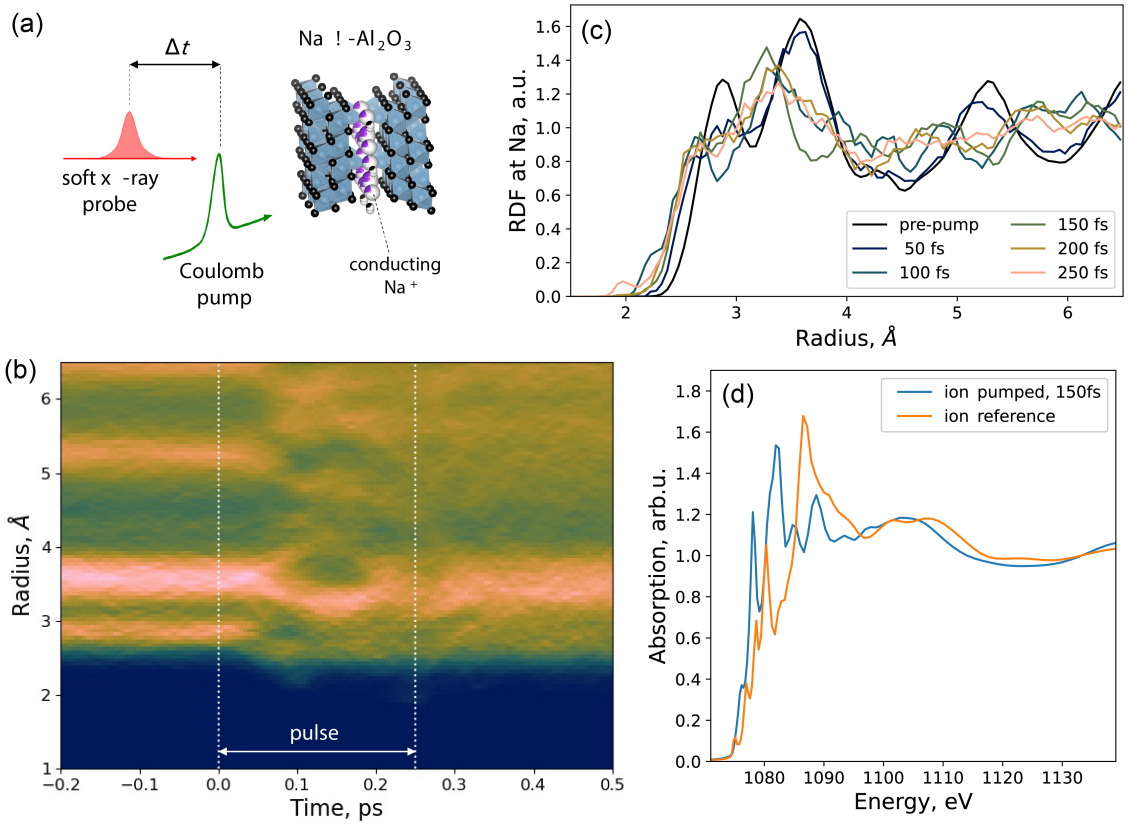

Fig. 6. Space-charge driven large-amplitude ionic motion of mobile Na^+ cations in the model ion conductor Na β alumina. (a) Proposed experiment setup where the terahertz-frequency field acts as a pump of ionic motion followed by a soft x-ray probe from the same FEL pulse. (b), (c) Simulated radial distribution function around the Na ions. Beyond 50 fs, the distribution is strongly perturbed by the space-charge field. (d) Simulated x-ray absorption spectra of one Na^+ ion compared with and without ("reference") the Coulomb-field perturbation.

This would enable a new view of the microscopic processes that underlie how ion motion occurs in rechargeable batteries and other electrochemical systems [88].

Applications include pure ionic conductors such as Na β/β'' aluminas [89,90], mixed ion-electron conductors such as layered-oxide cathodes Li(Ni, Mn, Co)O_2 [91,92] or $Na_2Mn_3O_7$ [93], quantum paraelectrics such as $SrTiO_3$ [86], and many others. Here, we simulate the pumping of the vibrations of conducting mobile Na^+ ions in Na β alumina [Fig. 6(a)]. The strongly anharmonic vibrations couple to translations called "hops" and ultimately to long-range ionic conduction, but this coupling remains challenging to both trigger and probe due to fluctuating potential-energy landscapes and the rarity of the hopping events [89]. The ionic response to a strong-field pump simulated with large-scale molecular dynamics [89,90,94,95] shows a substantially perturbed radial distribution function (RDF) around the mobile Na ions [Figs. 6(b) and 6(c)] due to their rapid displacements driven by the pump. The x-ray absorption spectrum of a representative ion computed in FEFF [96] (see Appendix A) based on the molecular-dynamics trajectory also shows strong changes relative to the same ion in an unperturbed material [Fig. 6(d)], in both near-edge and extended x-ray absorption fine structure (EXAFS) regions.

This simplified model suggests that core-level absorption spectroscopy can be used to track the ultrafast ionic motion driven by the strong field of the beam. Furthermore, since the time scales of lattice dynamics and especially metastable states accessed by strong-field excitations can extend much longer than the temporal length of the FEL pulses themselves, additional probes can be subsequently employed for multi-modal characterization of the dynamics triggered by the Coulomb pump.

5. CONCLUSION

In this paper, we have discussed how to produce and characterize ultrafast pump–probe fields at a FEL facility. By deliberately seeding coherent microbunches in an electron beam, we can create pairs of ultrashort current spikes. The tail spike generates sub-fs x-ray pulses that then slip ahead to overlap with the head spike, resulting in an intrinsically synchronized pump–probe scheme between x rays and the space-charge field of the beam.

We show that, compared to a conventional laser, the relativistic Coulomb field has unique properties that lend it to novel studies of ultrafast and strong-field dynamics. It can be compressed to attosecond pulse lengths and focused to atomic field strengths, all while supporting frequency content from 0 to 12 eV. Within this novel parameter space, we find that the beam can be used to explore ultrafast reaction pathways in photochemistry, to study opto-electronic proprieties of materials, and to drive large-amplitude nuclear motion. The combination of short pulses and large momentum transfer will allow the space-charge field to test the limits of material proprieties and improve our understanding of energy transfer on ultrafast time scales.

We support our assertion that an electron beam can be shaped to create both attosecond soft x-ray pulses and a powerful space-charge field by showing start-to-end simulations of the LCLS-II facility. The specificity of our example belies the flexibility of our technique. Indeed, a programmable laser heater can be used to etch complicated shapes into the electron beam current profile [55]. By synthesizing electric field transients with sub-femtosecond features, we can control the potential landscape and thus the dynamics of the resulting excitation [77–80]. And with the addition of a dedicated post-lasing compressor, we will be able to create high contrast current spikes capable of cleanly driving the impulsive excitation of valence electrons—a powerful method for wave packet control that has previously been available only to Rydberg electrons [74]. The opportunity not only to generate excited states, but also to control them and then probe them with soft x rays would open a new regime of attosecond physics possible at state-of-the-art XFELs.

APPENDIX A

X-ray absorption near edge spectra (XANES) at the Na K-edge were simulated for selected structural motifs of Na β/β'' alumina derived from classical molecular dynamics simulations of the electric field driven ion hopping process. The *ab initio* real-space multiple scattering method as implemented in the FEFF10 [96] code was employed for this purpose. Accordingly, cluster models of Na β/β'' alumina with ion configurations representative of both the un-perturbed and electric field perturbed systems were considered. In each case, the clusters ($10 \times 10 \times 10$ supercells) consisting of approximately 12,000 atoms were constructed centered on the XANES target Na ion of interest. Full multiple scattering (FMS) and self-consistent field (SCF) radii were both set to 9 Å around the reference Na site to ensure convergence in real space and to satisfy the convergence of spectra less than 10^{-3} arb. u. at each point.

Funding. Department of Energy, Office of Science, Basic Energy Sciences (DE-AC02-76SF00515).

Acknowledgment. A.K. gratefully acknowledges the Computing Center of the Far Eastern Branch of the Russian Academy of Sciences, 680000 Khabarovsk, Russia. The FEFF computations were carried out using the resources of the Center for Shared Use of Scientific Equipment "Center for Processing and Storage of Scientific Data of the Far Eastern Branch of the Russian Academy of Sciences" [97], funded by the Ministry of Science and Higher Education of the Russian Federation. We acknowledge many helpful conversations with David Reis concerning the application of strong beam driven fields to solids. This work was supported in part by the US DOE, Office of Science, Office of Basic Energy Sciences (BES), Accelerator and Detector Research program, and the DOE-BES Chemical Sciences, Geosciences, and Biosciences Division (CSGB).

Disclosures. The authors declare no competing interests.

Data availability. Data underlying the results presented in this paper are not publicly available at this time but may be obtained from the authors upon reasonable request.

REFERENCES AND NOTES

1. C. Bostedt, S. Boutet, D. M. Fritz, Z. Huang, H. J. Lee, H. T. Lemke, A. Robert, W. F. Schlotter, J. J. Turner, and G. J. Williams, "Linac Coherent Light Source: the first five years," Rev. Mod. Phys. **88**, 015007 (2016).
2. A. A. Lutman, R. Coffee, Y. Ding, Z. Huang, J. Krzywinski, T. Maxwell, M. Messerschmidt, and H.-D. Nuhn, "Experimental demonstration of femtosecond two-color x-ray free-electron lasers," Phys. Rev. Lett. **110**, 134801 (2013).
3. A. Marinelli, D. Ratner, A. A. Lutman, J. Turner, J. Welch, F.-J. Decker, H. Loos, C. Behrens, S. Gilevich, A. A. Miahnahri, S. Vetter, T. J. Maxwell, Y. Ding, R. Coffee, S. Wakatsuki, and Z. Huang, "High-intensity double-pulse x-ray free-electron laser," Nat. Commun. **6**, 6369 (2015).
4. A. A. Lutman, T. J. Maxwell, J. P. MacArthur, M. W. Guetg, N. Berrah, R. N. Coffee, Y. Ding, Z. Huang, A. Marinelli, S. Moeller, and J. C. U. Zemella, "Fresh-slice multicolour x-ray free-electron lasers," Nat. Photonics **10**, 745–750 (2016).
5. V. S. Petrović, M. Siano, J. L. White, *et al.*, "Transient x-ray fragmentation: probing a prototypical photoinduced ring opening," Phys. Rev. Lett. **108**, 253006 (2012).
6. J. P. Cryan, J. M. Glownia, J. Andreasson, *et al.*, "Auger electron angular distribution of double core-hole states in the molecular reference frame," Phys. Rev. Lett. **105**, 083004 (2010).
7. J. M. Glownia, J. Cryan, J. Andreasson, *et al.*, "Time-resolved pump-probe experiments at the LCLS," Opt. Express **18**, 17620–17630 (2010).
8. J. Duris, S. Li, T. Driver, *et al.*, "Tunable isolated attosecond x-ray pulses with gigawatt peak power from a free-electron laser," Nat. Photonics **14**, 30–36 (2020).
9. S. Li, T. Driver, P. Rosenberger, *et al.*, "Attosecond coherent electron motion in Auger-Meitner decay," Science **375**, 285–290 (2022).
10. Z. Zhang, A. S. Fisher, M. C. Hoffmann, B. Jacobson, P. S. Kirchmann, W.-S. Lee, A. Lindenberg, A. Marinelli, E. Nanni, R. Schoenlein, M. Qian, S. Sasaki, J. Xu, and Z. Huang, "A high-power, high-repetition-rate THz source for pump–probe experiments at Linac Coherent Light Source II," J. Synchrotron. Radiat. **27**, 890–901 (2020).
11. T. Koevener, "THz spectrometer calibration at FELIX," Ph.D. thesis (UniversitÃt Hamburg, 2016).
12. M. Ozerov, B. Bernáth, D. Kamenskyi, B. Redlich, A. F. G. van der Meer, P. C. M. Christianen, H. Engelkamp, and J. C. Maan, "A THz spectrometer combining the free electron laser FLARE with 33 T magnetic fields," Appl. Phys. Lett. **110**, 094106 (2017).
13. J. M. Bakker, V. J. F. Lapoutre, B. Redlich, J. Oomens, B. G. Sartakov, A. Fielicke, G. von Helden, G. Meijer, and A. F. G. van der Meer, "Intensity-resolved IR multiple photon ionization and fragmentation of C60," J. Chem. Phys. **132**, 074305 (2010).
14. L. Heting, H. Zhigang, W. Fangfang, *et al.*, "Hefei infrared free electron laser facility," Chin. J. Lasers **48**, 1700001 (2021).
15. J. M. Ortega, F. Glotin, and R. Prazeres, "Extension in far-infrared of the CLIO free-electron laser," Infrared Phys. Technol. **49**, 133–138 (2006).
16. K. Kawase, M. Nagai, K. Furukawa, M. Fujimoto, R. Kato, Y. Honda, and G. Isoyama, "Extremely high-intensity operation of a THz free-electron laser using an electron beam with a higher bunch charge," Nucl. Instrum. Methods Phys. Res. A **960**, 163582 (2020).
17. M. Shalaby and C. P. Hauri, "Demonstration of a low-frequency three-dimensional terahertz bullet with extreme brightness," Nat. Commun. **6**, 5976 (2015).
18. C. Vicario, A. V. Ovchinnikov, S. I. Ashitkov, M. B. Agranat, V. E. Fortov, and C. P. Hauri, "Generation of 0.9-mJ THz pulses in DSTMS pumped by a Cr:Mg_2SiO_4 laser," Opt. Lett. **39**, 6632–6635 (2014).
19. A. Sell, A. Leitenstorfer, and R. Huber, "Phase-locked generation and field-resolved detection of widely tunable terahertz pulses with amplitudes exceeding 100 MV/cm," Opt. Lett. **33**, 2767–2769 (2008).
20. X.-J. Wu, J.-L. Ma, B.-L. Zhang, S.-S. Chai, Z.-J. Fang, C.-Y. Xia, D.-Y. Kong, J.-G. Wang, H. Liu, C.-Q. Zhu, X. Wang, C.-J. Ruan, and Y.-T. Li, "Highly efficient generation of 0.2 mJ terahertz pulses in lithium niobate at room temperature with sub-50 fs chirped Ti:sapphire laser pulses," Opt. Express **26**, 7107–7116 (2018).
21. C. P. Hauri, C. Ruchert, C. Vicario, and F. Ardana, "Strong-field single-cycle THz pulses generated in an organic crystal," Appl. Phys. Lett. **99**, 161116 (2011).
22. J. A. Fülöp, Z. Ollmann, C. Lombosi, C. Skrobol, S. Klingebiel, L. Pálfalvi, F. Krausz, S. Karsch, and J. Hebling, "Efficient generation of THz pulses with 0.4 mJ energy," Opt. Express **22**, 20155–20163 (2014).
23. T. I. Oh, Y. S. You, N. Jhajj, E. W. Rosenthal, H. M. Milchberg, and K. Y. Kim, "Intense terahertz generation in two-color laser filamentation: energy scaling with terawatt laser systems," New J. Phys. **15**, 075002 (2013).
24. J. A. Fülöp, G. Polónyi, B. Monoszlai, G. Andriukaitis, T. Balciunas, A. Pugzlys, G. Arthur, A. Baltuska, and J. Hebling, "Highly efficient scalable monolithic semiconductor terahertz pulse source," Optica **3**, 1075–1078 (2016).

25. I. Dey, K. Jana, V. Y. Fedorov, A. D. Koulouklidis, A. Mondal, M. Shaikh, D. Sarkar, A. D. Lad, S. Tzortzakis, A. Couairon, and G. R. Kumar, "Highly efficient broadband terahertz generation from ultrashort laser filamentation in liquids," Nat. Commun. **8**, 1184 (2017).
26. J. W. Yoon, J. W. Yoon, Y. G. Kim, Y. G. Kim, I. W. Choi, I. W. Choi, J. H. Sung, J. H. Sung, H. W. Lee, S. K. Lee, S. K. Lee, S. K. Lee, C. H. Nam, C. H. Nam, and C. H. Nam, "Realization of laser intensity over 10^{23} W/cm^2," Optica **8**, 630–635 (2021).
27. M. J. Shaw, G. Bialolenker, G. J. Hirst, C. J. Hooker, M. H. Key, A. K. Kidd, J. M. D. Lister, K. E. Hill, G. H. C. New, and D. C. Wilson, "Ultrahigh-brightness laser beams with low prepulse obtained by stimulated Raman scattering," Opt. Lett. **18**, 1320–1322 (1993).
28. M. Mizoguchi, K. Kondo, and S. Watanabe, "100-fs, 10-Hz, terawatt KrF laser," J. Opt. Soc. Am. B **9**, 560–564 (1992).
29. H. Liang, P. Krogen, Z. Wang, H. Park, T. Kroh, K. Zawilski, P. Schunemann, J. Moses, L. F. DiMauro, F. X. Kärtner, and K.-H. Hong, "High-energy mid-infrared sub-cycle pulse synthesis from a parametric amplifier," Nat. Commun. **8**, 141 (2017).
30. F. Junginger, A. Sell, O. Schubert, B. Mayer, D. Brida, M. Marangoni, G. Cerullo, A. Leitenstorfer, and R. Huber, "Single-cycle multiterahertz transients with peak fields above 10 MV/cm," Opt. Lett. **35**, 2645–2647 (2010).
31. Y. Deng, A. Schwarz, H. Fattahi, M. Ueffing, X. Gu, M. Ossiander, T. Metzger, V. Pervak, H. Ishizuki, T. Taira, T. Kobayashi, G. Marcus, F. Krausz, R. Kienberger, and N. Karpowicz, "Carrier-envelope-phase-stable, 1.2 mJ, 1.5 cycle laser pulses at 2.1 um," Opt. Lett. **37**, 4973–4975 (2012).
32. G. Andriukaitis, T. Balčiūnas, S. Ališauskas, A. Pugžlys, A. Baltuška, T. Popmintchev, M.-C. Chen, M. M. Murnane, and H. C. Kapteyn, "90 GW peak power few-cycle mid-infrared pulses from an optical parametric amplifier," Opt. Lett. **36**, 2755–2757 (2011).
33. L. V. Grafenstein, M. Bock, D. Ueberschaer, E. Escoto, A. Koç, K. Zawilski, P. Schunemann, U. Griebner, and T. Elsaesser, "Multi-millijoule, few-cycle 5 μm OPCPA at 1 kHz repetition rate," Opt. Lett. **45**, 5998–6001 (2020).
34. U. Elu, T. Steinle, D. Sánchez, L. Maidment, K. Zawilski, P. Schunemann, U. D. Zeitner, C. Simon-Boisson, and J. Biegert, "Table-top high-energy 7 μm OPCPA and 260 mJ Ho:YLF pump laser," Opt. Lett. **44**, 3194–3197 (2019).
35. J. C. Travers, T. F. Grigorova, C. Brahms, and F. Belli, "High-energy pulse self-compression and ultraviolet generation through soliton dynamics in hollow capillary fibres," Nat. Photonics **13**, 547–554 (2019).
36. M. Ouillé, A. Vernier, F. Böhle, M. Bocoum, A. Jullien, M. Lozano, J.-P. Rousseau, Z. Cheng, D. Gustas, A. Blumenstein, P. Simon, S. Haessler, J. Faure, T. Nagy, and R. Lopez-Martens, "Relativistic-intensity near-single-cycle light waveforms at kHz repetition rate," Light Sci. Appl. **9**, 47 (2020).
37. D. E. Rivas, A. Borot, D. E. Cardenas, *et al.*, "Next generation driver for attosecond and laser-plasma physics," Sci. Rep. **7**, 5224 (2017).
38. D. Daranciang, J. Goodfellow, M. Fuchs, H. Wen, S. Ghimire, D. A. Reis, H. Loos, A. S. Fisher, and A. M. Lindenberg, "Single-cycle terahertz pulses with 0.2 V/å field amplitudes via coherent transition radiation," Appl. Phys. Lett. **99**, 141117 (2011).
39. Z. Wu, A. S. Fisher, J. Goodfellow, M. Fuchs, D. Daranciang, M. Hogan, H. Loos, and A. Lindenberg, "Intense terahertz pulses from SLAC electron beams using coherent transition radiation," Rev. Sci. Instrum. **84**, 022701 (2013).
40. J. A. Fülöp, S. Tzortzakis, and T. Kampfrath, "Laser-driven strong-field terahertz sources," Adv. Opt. Mater. **8**, 1900681 (2020).
41. HZDR, "THz FEL sources," (2022).
42. S. Szatmári, G. Marowsky, and P. Simon, "3.3 Femtosecond excimer lasers and their applications," in *Laser Systems, Part 1*, G. Herziger, H. Weber, and R. Poprawe, eds. (Springer Berlin Heidelberg, 2007), Vol. **11**, pp. 215–253.
43. In the cases where we did not extract focal-spot data [11,12,14–16, 28,31–33], we assume a transverse size (rms of intensity distribution) of $5\lambda/\pi$.
44. S. M. Seltzer, "Cross sections for bremsstrahlung production and electron-impact ionization," in *Monte Carlo Transport of Electrons and Photons*, T. M. Jenkins, W. R. Nelson, and A. Rindi, eds. Ettore Majorana International Science Series, (Springer US, 1988), pp. 81–114.
45. P. Krejcik, F. J. Decker, P. Emma, K. Hacker, L. Hendrickson, C. L. O'Connell, H. Schlarb, H. Smith, and M. Stanek, "Commissioning of the SPPS linac bunch compressor," in *Proceedings of the Particle Accelerator Conference* (2003), p. 3.
46. C. I. Clarke, F. J. Decker, R. Erikson, C. Hast, M. J. Hogan, R. Iverson, S. Z. Li, Y. Nosochkov, N. Phinney, J. Sheppard, U. Wienands, M. Woodley, G. Yocky, M. Park, A. Seryi, and W. Wittmer, "FACET: the new user facility at SLAC," SLAC-PUB-14563 (2011), p. 3.
47. I. Tudosa, C. Stamm, A. B. Kashuba, F. King, H. C. Siegmann, J. Stöhr, G. Ju, B. Lu, and D. Weller, "The ultimate speed of magnetic switching in granular recording media," Nature **428**, 831–833 (2004).
48. Y. Lu, A. Alvarez, C.-H. Kao, J.-S. Bow, S.-Y. Chen, and I.-W. Chen, "An electronic silicon-based memristor with a high switching uniformity," Nat. Electron. **2**, 66–74 (2019).
49. B. D. O'Shea, G. Andonian, S. K. Barber, C. I. Clarke, P. D. Hoang, M. J. Hogan, B. Naranjo, O. B. Williams, V. Yakimenko, and J. B. Rosenzweig, "Conductivity induced by high-field terahertz waves in dielectric material," Phys. Rev. Lett. **123**, 134801 (2019).
50. Z. Zhang, J. Duris, J. P. MacArthur, Z. Huang, and A. Marinelli, "Double chirp-taper x-ray free-electron laser for attosecond pump-probe experiments," Phys. Rev. Accel. Beams **22**, 050701 (2019).
51. J. P. MacArthur, J. Duris, Z. Zhang, A. Lutman, A. Zholents, X. Xu, Z. Huang, and A. Marinelli, "Phase-stable self-modulation of an electron beam in a magnetic wiggler," Phys. Rev. Lett. **123**, 214801 (2019).
52. H.-S. Kang, C.-K. Min, H. Heo, *et al.*, "Hard x-ray free-electron laser with femtosecond-scale timing jitter," Nat. Photonics **11**, 708–713 (2017).
53. N. Hartmann, W. Helml, A. Galler, *et al.*, "Sub-femtosecond precision measurement of relative X-ray arrival time for free-electron lasers," Nat. Photonics **8**, 706–709 (2014).
54. M. Woodley, "LCLS lattice description," (2019).
55. D. Cesar, A. Anakru, S. Carbajo, J. Duris, P. Franz, S. Li, N. Sudar, Z. Zhang, and A. Marinelli, "Electron beam shaping via laser heater temporal shaping," Phys. Rev. Accel. Beams **24**, 110703 (2021).
56. J. Qiang, Y. Ding, P. Emma, Z. Huang, D. Ratner, T. O. Raubenheimer, M. Venturini, and F. Zhou, "Start-to-end simulation of the shot-noise driven microbunching instability experiment at the Linac Coherent Light Source," Phys. Rev. Accel. Beams **20**, 054402 (2017).
57. L. Wang, P. Emma, J. Qiang, and T. Raubenheimer, "Benchmark of ELEGANT and IMPACT," in *Proceedings of the 37th International Free Electron Laser Conference FEL2015* (JACoW, 2015), p. 3.
58. M. Borland, "ELEGANT: A flexible SDDS-compliant code for accelerator simulation," Tech. Rep. LS-287 (Argonne National Laboratory, 2000).
59. S. Reiche, "GENESIS 1.3: a fully 3D time-dependent FEL simulation code," Nucl. Instrum. Methods Phys. Res. A **429**, 243–248 (1999).
60. F. Robicheaux and L. D. Noordam, "Coherent scattering with pulsed matter beams," Phys. Rev. Lett. **84**, 3735–3739 (2000).
61. S. B. van der Geer, O. J. Luiten, M. J. de Loos, G. Pöplau, and U. van Rienen, "3D space-charge model for GPT simulations of high brightness electron bunches," in *Institute of Physics Conference Series* No. 175 (2005), p. 101.
62. M. Guerra, F. Parente, P. Indelicato, and J. P. Santos, "Modified binary encounter Bethe model for electron-impact ionization," Int. J. Mass Spectrom. **313**, 1–7 (2012).
63. I. Orfanos, I. Makos, I. Liontos, E. Skantzakis, B. Förg, D. Charalambidis, and P. Tzallas, "Attosecond pulse metrology," APL Photon. **4**, 080901 (2019).
64. J. Itatani, F. Quéré, G. L. Yudin, M. Y. Ivanov, F. Krausz, and P. B. Corkum, "Attosecond streak camera," Phys. Rev. Lett. **88**, 173903 (2002).
65. M. Drescher, M. Hentschel, R. Kienberger, G. Tempea, C. Spielmann, G. A. Reider, P. B. Corkum, and F. Krausz, "X-ray pulses approaching the attosecond frontier," Science **291**, 1923–1927 (2001).
66. Y. Mairesse and F. Quéré, "Frequency-resolved optical gating for complete reconstruction of attosecond bursts," Phys. Rev. A **71**, 011401 (2005).
67. J. Gagnon, E. Goulielmakis, and V. Yakovlev, "The accurate FROG characterization of attosecond pulses from streaking measurements," Appl. Phys. B **92**, 25–32 (2008).
68. M. Chini, S. Gilbertson, S. D. Khan, and Z. Chang, "Characterizing ultrabroadband attosecond lasers," Opt. Express **18**, 13006–13016 (2010).
69. P. D. Keathley, S. Bhardwaj, J. Moses, G. Laurent, and F. X. Kärtner, "Volkov transform generalized projection algorithm for attosecond pulse characterization," New J. Phys. **18**, 073009 (2016).
70. D. C. Haynes, M. Wurzer, A. Schletter, *et al.*, "Clocking Auger electrons," Nat. Phys. **17**, 512–518 (2021).

71. N. Hartmann, G. Hartmann, R. Heider, *et al.*, "Attosecond time–energy structure of x-ray free-electron laser pulses," Nat. Photonics **12**, 215–220 (2018).
72. R. Heider, M. S. Wagner, N. Hartmann, *et al.*, "Megahertz-compatible angular streaking with few-femtosecond resolution at x-ray free-electron lasers," Phys. Rev. A **100**, 053420 (2019).
73. S. Li, Z. Guo, R. N. Coffee, K. Hegazy, Z. Huang, A. Natan, T. Osipov, D. Ray, A. Marinelli, and J. P. Cryan, "Characterizing isolated attosecond pulses with angular streaking," Opt. Express **26**, 4531–4547 (2018).
74. R. R. Jones, D. You, and P. H. Bucksbaum, "Ionization of Rydberg atoms by subpicosecond half-cycle electromagnetic pulses," Phys. Rev. Lett. **70**, 1236–1239 (1993).
75. N. Tsatrafyllis, B. Bergues, H. Schröder, L. Veisz, E. Skantzakis, D. Gray, B. Bodi, S. Kuhn, G. D. Tsakiris, D. Charalambidis, and P. Tzallas, "The ion microscope as a tool for quantitative measurements in the extreme ultraviolet," Sci. Rep. **6**, 21556 (2016).
76. V. Yakimenko, L. Alsberg, E. Bong, G. Bouchard, C. Clarke, C. Emma, S. Green, C. Hast, M. J. Hogan, J. Seabury, N. Lipkowitz, B. O'Shea, D. Storey, G. White, and G. Yocky, "FACET-II facility for advanced accelerator experimental tests," Phys. Rev. Accel. Beams **22**, 101301 (2019).
77. Y. Arasaki and K. Takatsuka, "Optical conversion of conical intersection to avoided crossing," Phys. Chem. Chem. Phys. **12**, 1239–1242 (2010).
78. Y. Arasaki, K. Wang, V. McKoy, and K. Takatsuka, "Monitoring the effect of a control pulse on a conical intersection by time-resolved photoelectron spectroscopy," Phys. Chem. Chem. Phys. **13**, 8681–8689 (2011).
79. M. Richter, F. Bouakline, J. González-Vázquez, L. Martínez-Fernández, I. Corral, S. Patchkovskii, F. Morales, M. Ivanov, F. Martín, and O. Smirnova, "Sub-laser-cycle control of coupled electron–nuclear dynamics at a conical intersection," New J. Phys. **17**, 113023 (2015).
80. M. Richter, J. González-Vázquez, Z. Mašín, D. S. Brambila, A. G. Harvey, F. Morales, and F. Martín, "Ultrafast imaging of laser-controlled nonadiabatic dynamics in NO_2 from time-resolved photoelectron emission," Phys. Chem. Chem. Phys. **21**, 10038–10051 (2019).
81. M. W. Guetg, B. Beutner, E. Prat, and S. Reiche, "Optimization of free electron laser performance by dispersion-based beam-tilt correction," Phys. Rev. Spec. Top. Accel. Beams **18**, 030701 (2015).
82. L. Yue and M. B. Gaarde, "Introduction to theory of high-harmonic generation in solids: tutorial," J. Opt. Soc. Am. B **39**, 535–555 (2022).
83. P. G. Hawkins, M. Y. Ivanov, and V. S. Yakovlev, "Effect of multiple conduction bands on high-harmonic emission from dielectrics," Phys. Rev. A **91**, 013405 (2015).
84. S. Y. Kruchinin, M. Korbman, and V. S. Yakovlev, "Theory of strong-field injection and control of photocurrent in dielectrics and wide band gap semiconductors," Phys. Rev. B **87**, 115201 (2013).
85. P. Salén, M. Basini, S. Bonetti, J. Hebling, M. Krasilnikov, A. Y. Nikitin, G. Shamuilov, Z. Tibai, V. Zhaunerchyk, and V. Goryashko, "Matter manipulation with extreme terahertz light: progress in the enabling THz technology," Phys. Rep. **836–837**, 1–74 (2019).
86. X. Li, T. Qiu, J. Zhang, E. Baldini, J. Lu, A. M. Rappe, and K. A. Nelson, "Terahertz field–induced ferroelectricity in quantum paraelectric $SrTiO_3$," Science **364**, 1079–1082 (2019).
87. A. de la Torre, D. M. Kennes, M. Claassen, S. Gerber, J. W. McIver, and M. A. Sentef, "Colloquium: nonthermal pathways to ultrafast control in quantum materials," Rev. Mod. Phys. **93**, 041002 (2021).
88. A. Sood, A. D. Poletayev, D. A. Cogswell, P. M. Csernica, J. T. Mefford, D. Fraggedakis, M. F. Toney, A. M. Lindenberg, M. Z. Bazant, and W. C. Chueh, "Electrochemical ion insertion from the atomic to the device scale," Nat. Rev. Mater. **6**, 847–867 (2021).
89. A. D. Poletayev, M. C. Hoffmann, J. A. Dawson, S. W. Teitelbaum, M. Trigo, M. S. Islam, and A. M. Lindenberg, "The persistence of memory in ionic conduction probed by nonlinear optics," arXiv, arXiv:2110.06522 [cond-mat, physics:physics] (2021).
90. A. D. Poletayev, J. A. Dawson, M. S. Islam, and A. M. Lindenberg, "Defect-driven anomalous transport in fast-ion conducting solid electrolytes," Nat. Mater. **21**, 1066–1073 (2022).
91. R. A. House, G. J. Rees, M. A. Pérez-Osorio, J.-J. Marie, E. Boivin, A. W. Robertson, A. Nag, M. Garcia-Fernandez, K.-J. Zhou, and P. G. Bruce, "First-cycle voltage hysteresis in Li-rich 3D cathodes associated with molecular O_2 trapped in the bulk," Nat. Energy **5**, 777–785 (2020).
92. W. E. Gent, I. I. Abate, W. Yang, L. F. Nazar, and W. C. Chueh, "Design rules for high-valent redox in intercalation electrodes," Joule **4**, 1369–1397 (2020).
93. I. I. Abate, C. D. Pemmaraju, S. Y. Kim, K. H. Hsu, S. Sainio, B. Moritz, J. Vinson, M. F. Toney, W. Yang, W. E. Gent, T. P. Devereaux, L. F. Nazar, and W. C. Chueh, "Coulombically-stabilized oxygen hole polarons enable fully reversible oxygen redox," Energy Environ. Sci. **14**, 4858–4867 (2021).
94. P. K. Mishra, O. Vendrell, and R. Santra, "Ultrafast energy transfer from solvent to solute induced by subpicosecond highly intense THz pulses," J. Phys. Chem. B **119**, 8080–8086 (2015).
95. P. K. Mishra, V. Bettaque, O. Vendrell, R. Santra, and R. Welsch, "Prospects of using high-intensity THz pulses to induce ultrafast temperature-jumps in liquid water," J. Phys. Chem. A **122**, 5211–5222 (2018).
96. J. J. Kas, F. D. Vila, C. D. Pemmaraju, T. S. Tan, and J. J. Rehr, "Advanced calculations of x-ray spectroscopies with FEFF10 and Corvus," J. Synchrotron. Radiat. **28**, 1801–1810 (2021).
97. A. A. Sorokin, S. V. Makogonov, and S. P. Korolev, "The information infrastructure for collective scientific work in the Far East of Russia," Sci. Tech. Inf. Process. **44**, 302–304 (2017).